

Four Lectures on the Physics of Crystal Growth

Joachim Krug

Fachbereich Physik, Universität Essen, 45117 Essen, Germany

Abstract

Several aspects of the theory of epitaxial crystal growth from atomic or molecular beams are developed from the perspective of statistical physics. Lectures are devoted to the rate equation theory of two-dimensional nucleation and its limitations; the growth of multilayer wedding cakes in the presence of strong step edge barriers; the continuum theory of mound coarsening; and growth-induced step meandering on vicinal surfaces.

Key words: Crystal growth, nucleation, pattern formation, phase ordering, surface instabilities, surface diffusion, vicinal surfaces

PACS: 81.10.Aj, 05.40.-a, 68.55.-a

1 Introduction

The growth of a crystalline film from a molecular or atomic beam, commonly referred to as Molecular Beam Epitaxy (MBE), is a simple example of a self-assembly process. In contrast to crystallization from the melt, which often leads to dendrites and other ramified patterns [1], MBE growth can be described without reference to the transport of matter, latent heat or impurities in the fluid phase. The remarkable richness of patterns forming during MBE is determined solely by processes which occur locally at the surface. Moreover, in the case of *homoepitaxial* growth, in which a film is grown on a substrate of the same material, energetic determinants such as interfacial free energies and misfit strain are absent, so that the film morphology is governed primarily by growth kinetics. This makes homoepitaxy an ideal laboratory in which to study the emergence of mesoscopic patterns and their associated length scales through self-organization processes far from equilibrium. An additional benefit is that, since the invention of scanning tunneling microscopy, this laboratory is open to direct visual inspection.

The main steps in the growth process can be summarized as follows¹. Atoms are deposited at rate F . They migrate along the surface with a two-dimensional diffusion coefficient D . When two atoms meet they form a dimer. Dimers may subsequently disintegrate, or they may grow by aggregation of further atoms into trimers and larger clusters. Once a substantial fraction of the surface is covered by two-dimensional island clusters, these begin to coalesce and a full atomic layer forms, on which the processes involved in producing the first layer repeat themselves.

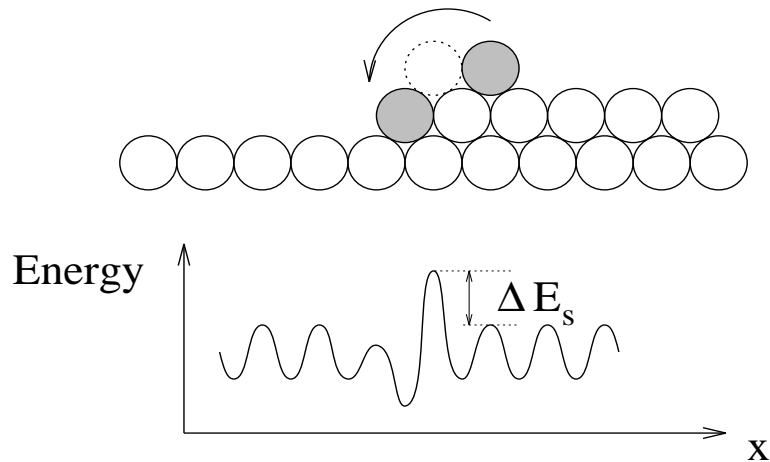


Fig. 1. An atom descending from a step edge experiences an additional energy barrier ΔE_s .

At this stage of the growth process, the fate of atoms deposited on top of first layer islands becomes important. Such atoms may either descend from the island, thus contributing to the growth of the island edge, or they may remain on the island, promoting the nucleation of the next layer. On many crystal surfaces, the diffusion of atoms between different atomic layers is suppressed due to additional energy barriers, which an atom crossing a step has to overcome. This phenomenon was first observed experimentally by Ehrlich and Hudda [2], and some of its consequences for the growth of stepped surfaces were analyzed by Schwoebel and Shipsey [3]. The atomistic origin of the additional step edge barrier is illustrated in Figure 1: An atom descending from a step edge passes through a transition state of very low coordination, which implies poor binding and thus a higher energy. This picture is oversimplified, because in many cases descent by concerted exchange is more facile than hopping [4]. Nevertheless, it is generally true that the rate for interlayer diffusion, in the following denoted by D' , is smaller than the in-layer diffusion constant D .

In-layer and interlayer diffusion, as well as all other atomic processes involved

¹ Throughout these notes, the unit of length will be the substrate lattice spacing. Thus the deposition rate F denotes the number of atoms deposited per unit time and adsorption site, and the diffusion coefficients D and D' are actually hopping rates. All three quantities have units of inverse time.

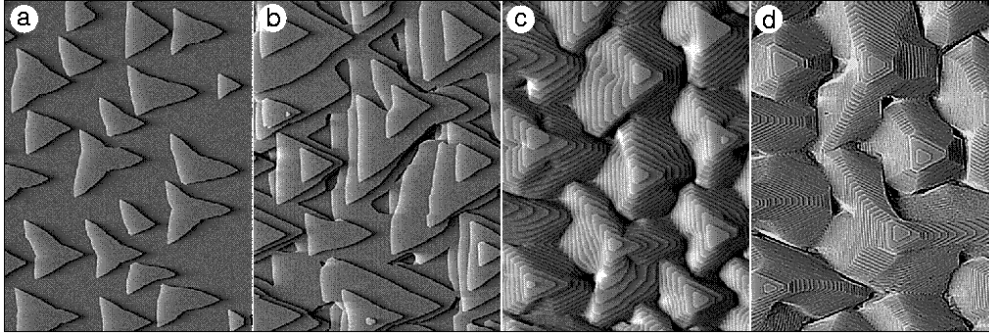


Fig. 2. Growth of Pt on Pt(111) at $T = 440\text{K}$ [5]. The total coverage is (a) 0.3 monolayers (ML), (b) 3 ML, (c) 12 ML and (d) 90 ML. The image size is $2600\text{\AA} \times 3450\text{\AA}$. Courtesy of T. Michely.

in the growth, decay and shape changes of two-dimensional islands, are *thermally activated*. Let us recall what this means, using the in-layer migration process as illustration. To a good approximation, the motion of an adsorbed atom (an *adatom*) on a crystal surface can be viewed as a two-dimensional random walk between adsorption sites. In hopping from one adsorption site to another, the adatom has to overcome an energy barrier E_D . The energy is provided by thermal substrate vibrations. This implies the familiar Arrhenius form

$$D = D_0 e^{-E_D/k_B T} \quad (1)$$

for the diffusion coefficient. In (1), T is the substrate temperature, k_B the Boltzmann constant, and D_0 is an attempt frequency with a typical magnitude around 10^{13}s^{-1} . The main role of temperature in MBE growth is that it regulates, through expressions like (1), the relative rates of the different activated processes on the surface.

In these lectures we will explore some of the pattern forming phenomena that arise through the interplay of the three kinetic rates D , D' and F . In Section 2, the classical atomistic rate equation theory of two-dimensional nucleation will be briefly reviewed. Its central result is a scaling law, Eq.(12), which relates the spacing between first layer island clusters to the ratio D/F . The limitations of the classical theory become evident in the treatment of nucleation on top of islands, which requires statistical arguments beyond rate equations. Sections 3 and 4 are devoted to the mound patterns which appear generically in multilayer growth (see Figure 2 for an example). The approach taken in Section 3 is quite atomistic, focusing on the distribution of the deposited mass among the different layers and the corresponding mound shapes. Section 4 provides a more macroscopic perspective, which allows one to address also the mass transport between mounds and the coarsening of the pattern. The final Section 5 is devoted to growth on vicinal surfaces, which are intrinsically anisotropic due to the presence of preexisting steps.

The treatment of these topics is far from exhaustive. More details can be found in several recent books and review articles [6–12]. The lectures do not cover the theory of kinetic roughening by stochastic fluctuations, which in fact initiated, through the seminal work of Kardar, Parisi and Zhang [13], the interest of the statistical physics community in film growth. The reasons for this omission are twofold. First, the subject has been extensively reviewed elsewhere [11,12,14,15]. Second, despite its tremendous conceptual impact, the relevance of kinetic roughening theory to real film growth has still not been quantitatively demonstrated². This is in contrast to the growth instabilities discussed in the present lectures, where a quantitative linking of mesoscopic patterns to specific atomistic processes appears to be well within reach. A possible manifestation of kinetic roughening in a setting which is relevant to MBE growth is the noise-induced damping of growth oscillations in layer-by-layer growth. Here kinetic roughening theory has been used to establish scaling relationships between the damping time and the ratio D/F [11,17–19].

2 Two-dimensional nucleation

The formation of an atomic layer on a high symmetry substrate without steps or defects has to proceed through the congregation of mobile adatoms into stable clusters, which subsequently grow by accretion. The process is analogous to the nucleation of a condensed phase out of a supersaturated gas, as described by thermodynamic nucleation theory [20]. The central object of this theory is the *critical nucleus*, which defines the free energy barrier that has to be surmounted to reach the stable phase. The size of the critical nucleus is inversely proportional to the supersaturation.

In far from equilibrium growth the critical nucleus size may reach atomic dimensions, thus precluding a straightforward application of thermodynamic concepts and necessitating the development of an *atomistic* theory of nucleation kinetics [21]. This was achieved in the 1960's and 70's by Zinsmeister, Stowell, Venables and others; extensive reviews are available [22–24]. Precise experimental tests of the theory have become possible only recently [25,26]. In addition, large scale computer simulations play an increasingly important rôle in establishing the validity and limitations of nucleation theory, as they allow for separate scrutiny of the various assumptions going into the theory.

The atomistic theory of two-dimensional nucleation is summarized in the next section. We then turn to the problem of second layer nucleation on top of islands, which differs from the nucleation of the first layer because of the confinement of the atoms by step edge barriers. This problem is of conceptual

² Experimental work until 1995 has been reviewed in [16].

interest because it illustrates the limitations of mean field rate equation theory [27–29]. At the same time a quantitative theory of second layer nucleation is a necessary prerequisite for the discussion of multilayer growth in the subsequent lectures.

2.1 Rate equation theory

The classical approach to nucleation kinetics starts from balance or rate equations for the areal concentrations n_s of clusters consisting of s atoms; n_1 is the adatom density, n_2 the density of dimers, and so on. To be precise, we define n_s as the number of clusters per surface area, averaged over a region containing a large number of clusters. If the adatoms are the only mobile species (the mobility of larger clusters is negligibly small), then clusters grow solely by aggregation of single adatoms. Defining Γ_s to be the net rate at which $s + 1$ -clusters form from s -clusters, we have for $s \geq 2$

$$\frac{dn_s}{dt} = \Gamma_{s-1} - \Gamma_s \quad (s \geq 2). \quad (2)$$

The net formation rates Γ_s can be written as

$$\Gamma_s = \sigma_s D n_1 n_s - \gamma_{s+1} n_{s+1}, \quad (3)$$

where γ_s is the rate at which adatoms detach from a s -cluster and the dimensionless *capture number* σ_s accounts for the propensity of a s -cluster to absorb an adatom (see below). The chain (2) of aggregation equations is fed by the adatom density n_1 . If desorption from the surface can be neglected (the *complete condensation* limit [22,24]), adatoms are lost only through dimer formation and capture at larger clusters, and the adatom rate equation reads

$$\frac{dn_1}{dt} = F - 2\Gamma_1 - \sum_{s \geq 2} \Gamma_s. \quad (4)$$

The deposition rate F is defined as the number of atoms arriving per unit time and surface area.

In principle, Eqs.(2-4) provide a complete description of the nucleation process; in practice, they contain far too many (generally unknown) kinetic parameters to be useful. This difficulty is commonly circumvented by introducing a distinction between stable and unstable clusters, and postulating a separation of time scales between the kinetics of the two kinds. Stable clusters of sizes $s \geq i^* + 1$ are assumed not to decay, i.e. $\gamma_s = 0$ for $s \geq i^*$, while the detachment

of adatoms from unstable clusters with $s \leq i^*$ occurs sufficiently rapidly to establish thermodynamic equilibrium between the different size populations. It is important to note that, in contrast to thermodynamic nucleation theory, the critical cluster size i^* introduced here contains a *kinetic* element, as it refers to stability and equilibration only on the time scale relevant to the deposition experiment.

Next the total density N of stable clusters, also referred to as *islands* in the following, is introduced through

$$N = \sum_{s=i^*+1}^{\infty} n_s. \quad (5)$$

Summing (2) from $s = i^* + 1$ this is seen to evolve according to

$$\frac{dN}{dt} = \sigma_{i^*} D n_1 n_{i^*}. \quad (6)$$

The assumption of thermal equilibrium among unstable clusters implies that the net formation rates Γ_s vanish for $1 \leq s \leq i^* - 1$, and induces the detailed balance relations [21]

$$n_s \approx n_1^s e^{E_s/k_B T} \quad (2 \leq s \leq i^*) \quad (7)$$

between the unstable cluster concentrations and the adatom concentration. Here E_s is the total (positive) binding energy of an s -cluster, i.e. the energy needed to disperse the cluster into single adatoms; note that $E_1 = 0$.

Using (7) the nucleation rate on the right hand side of (6) can be expressed in terms of the adatom density. To complete the description, the rate equation for n_1 is simplified by introducing the average capture number for stable islands

$$\bar{\sigma} = N^{-1} \sum_{s=i^*+1}^{\infty} n_s \sigma_s. \quad (8)$$

Equation (4) can then be written in the form

$$\frac{dn_1}{dt} = F - \sigma_{i^*} D n_1 n_{i^*} - \bar{\sigma} D n_1 N. \quad (9)$$

Together (6), (7) and (9) form a closed set of equations from which the island and adatom densities can be computed.

Before turning to the solution of these equations, some remarks concerning the capture numbers σ_s are in order. In the early literature on atomistic nucleation theory, a geometric view of the capture numbers as effective cross sections for atoms colliding with clusters prevailed. More appropriately, they are defined through the requirement that the flux of adatoms to a cluster of size s should be, on average, equal to $\sigma_s D n_1$. The capture number of a cluster evidently depends on its size, but in general it depends on the sizes and locations of surrounding clusters as well, because these affect the adatom concentration field. The calculation of σ_s involves the solution of a diffusion equation for the adatom concentration, with appropriate boundary conditions representing both the capture of adatoms at the cluster of interest, and the presence of other clusters far away [30]. In this sense the capture numbers retain some information about the spatial arrangement of the clusters, which is otherwise not accounted for in the rate equations; in the jargon of statistical mechanics, the rate equation description constitutes a *mean field* approximation. In practice, both σ_{i^*} and $\bar{\sigma}$ turn out to be slowly varying functions which can be replaced by constants for many (though not all) purposes. We adopt this simplification for the present discussion.

The solutions of the coupled equations (6) and (9) display two temporal regimes. In the early time, *transient* nucleation regime the loss terms on the right hand side of (9) are negligible. The adatom concentration increases proportional to the total coverage $\Theta = Ft$, and the island density grows rapidly as $N \sim \Theta^{i^*+2}$. This regime ends when capture of adatoms at stable islands becomes appreciable, at a coverage which can be estimated by comparing the first and last terms on the right hand side of (9). In the subsequent *steady state* regime these two terms balance completely, and the adatom density is determined by the island density through

$$n_1 \approx \frac{F}{D\bar{\sigma}N}. \quad (10)$$

Inserting this into (6,7) and integrating in time yields the central result of nucleation theory,

$$N \approx \Theta^{1/(i^*+2)} \left(\frac{F}{D}\right)^{\frac{i^*}{i^*+2}} e^{E_{i^*}/(i^*+2)k_B T}. \quad (11)$$

The most important feature of this expression is that it takes the form of a *scaling relation*

$$N \sim \left(\frac{F}{D}\right)^x \quad (12)$$

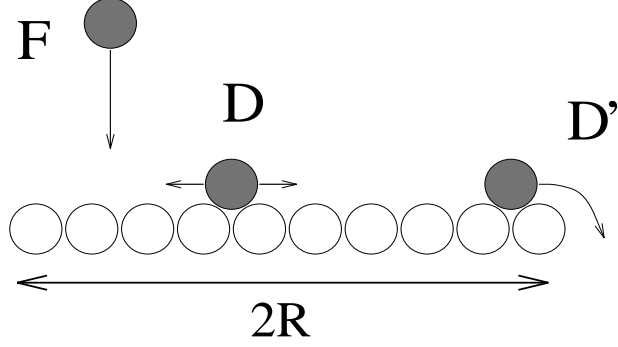


Fig. 3. Kinetic processes involved in second layer nucleation. The figure shows a circular island viewed from the side.

between the island number density and the ratio of the two basic kinetic rates D and F of the deposition process, with the *scaling exponent* χ taking the value $\chi = i^*/(i^* + 2)$ (for a generalized expression see (24)).

The rate equations formulated above are restricted to the low coverage regime, since finite coverage effects such as direct impingement and cluster-cluster coalescence have been neglected. In the absence of cluster mobility, coalescence provides the only mechanism by which the island density can decrease. This produces a maximum in $N(\Theta)$ which is often used as a convenient reference point for the experimental determination of cluster densities.

2.2 The rate of second layer nucleation

We now ask how the nucleation process is modified when it occurs on top of an island, rather than on the (unbounded) substrate. The geometry is illustrated in Figure 3. Atoms are being deposited at rate F onto a circular island of radius R . They diffuse on the island with an in-layer diffusion constant D , and descend from it with an (average) interlayer diffusion rate $D' < D$. We are looking for the probability per unit time, ω , for a nucleation event to occur on the island. Assuming that dimers of adsorbed atoms are stable (as they will be at sufficiently low temperatures), nucleation takes place as soon as two adatoms meet. In the terminology of the preceding subsection, this corresponds to $i^* = 1$; for a generalization of the following considerations to $i^* > 1$ see [29].

The kinetic rates F , D and D' combine to form three relevant time scales: The *interarrival time*

$$\Delta t = \frac{1}{\pi R^2 F} \quad (13)$$

between subsequent depositions onto the island; the *diffusion time*

$$\tau_D \sim R^2/D \quad (14)$$

required for an atom to diffuse once across the island, or for two atoms to meet; and the *residence time* τ which an atom spends on the island before descending, when no nucleation event takes place. The calculation of the residence time requires the solution of a stationary diffusion problem with appropriate boundary conditions at the step edge, which yields [27,31]

$$\tau = \frac{R^2}{8D} + \frac{R}{2D'}. \quad (15)$$

The residence time is comparable to the diffusion time τ_D if the suppression of interlayer transport is weak, in the sense that $D/D' \ll R$, while in the opposite regime of *strong step edge barriers*, $D/D' \gg R$, the residence time becomes $\tau = R/2D'$ independent of ν .

We will focus on the latter regime in the following. Then $\tau \gg \tau_D$, which implies that two atoms are certain to meet once they are present simultaneously on the island. The probability for this to occur is $\tau/(\tau + \Delta t) \approx \tau/\Delta t$ if $\Delta t \gg \tau$, which is true for reasonable deposition fluxes. Multiplying this by the total number of atoms deposited onto the island per unit time, we obtain the expression [27]

$$\omega = \frac{\tau}{(\Delta t)^2} = \frac{\pi^2 F^2 R^5}{2D'} \quad (16)$$

for the nucleation rate, which is *exact* under the stated conditions.

2.3 The limitations of mean field nucleation theory

The first calculation of the rate of second layer nucleation [31] was based on the rate equation (6), in which the average adatom density n_1 is replaced by its local value $n(\vec{r})$ at a point \vec{r} on the island. The *local* nucleation rate $I(\vec{r})$, which counts the number of nucleation events per time and lattice site, is then given by

$$I(\vec{r}) = \sigma_{i^*} D e^{E_{i^*}/k_B T} n(\vec{r})^{i^*+1}. \quad (17)$$

Computing the adatom density profile from the stationary diffusion equation and integrating over the island area, the total nucleation rate on a circular

island is obtained. Comparison with the exact expression (16) for $i^* = 1$ shows that the rate equation approach overestimates (16) by a factor of the order of $D/RD' \gg 1$ [27].

To elucidate the origin of this discrepancy, it is useful to view the encounter of the two atoms as a first passage problem in the four-dimensional space spanned by their coordinates. The joint diffusion of the atoms stops either when the two reach adjacent lattice sites (nucleation) or when one of them escapes, whatever happens first. The detailed analysis of this process [32] reveals the nature of the approximation based on (17): Setting the nucleation rate proportional to the square of the adatom density amounts to treating the atoms as *noninteracting*, in the sense that they are allowed to continue their diffusion even after they have met; in this way a single pair can accumulate several (spurious) nucleation events, and the nucleation rate is overestimated.

For a quantitative comparison, we note that (for $i^* = 1$) the nucleation probability p_{nuc} per atom can be written quite generally as the product of the (mean) adatom density and the number $N_{\text{dis}}(\tau)$ of *distinct* sites the atom encounters during its lifetime [33]. The validity of this statement becomes evident by assuming that all other adatoms are immobile: Then it is clear that repeated visits to the same unoccupied site do not increase the chance for nucleation. The lifetime of the atom equals its residence time in the case of second layer nucleation, but the argument applies equally well to the nucleation of the first layer, where the lifetime is determined by capture at stable islands, see below.

Using the general relation [27]

$$\tau = \bar{n}/F \tag{18}$$

between the residence time and the mean adatom density \bar{n} , which follows from simple mass balance considerations, the total nucleation rate on the island can then be written as

$$\omega = (\Delta t)^{-1} p_{\text{nuc}} = F N_{\text{dis}} \frac{\tau}{\Delta t}. \tag{19}$$

In the strong barrier limit, N_{dis} equals the total number of sites on the island, and (19) reproduces (16). To compare (19) to the rate equation approximation, we multiply the local nucleation rate (17) by the island area and obtain, in order of magnitude,

$$\omega_{\text{mf}} \sim R^2 D (\bar{n})^2 \sim F N_{\text{all}} \frac{\tau}{\Delta t}, \tag{20}$$

where (18) has been used, and the number $N_{\text{all}} = D\tau$ of *all* sites visited by an adatom during its residence has been introduced. Thus the expressions (19)

and (20) differ, in general, by a factor $N_{\text{all}}/N_{\text{dis}} > 1$.

The distinction between N_{all} and N_{dis} affects also the mean field calculation of the density of first layer islands in Section 2.1 [33]. In this case the life time of a freshly deposited adatom is of the order $\tau \sim 1/(ND)$, and the average adatom density is $n_1 = F\tau \sim F/ND$, compare to (10). The theory of two-dimensional random walks provides the expression $N_{\text{dis}} \approx \pi D\tau/\ln(D\tau)$ for $D\tau \gg 1$ [34]. The actual value of N is fixed by the requirement that, out of the approximately $1/N$ adatoms deposited in the area occupied by one island, only one (or two!) forms a nucleus, i.e. that $p_{\text{nuc}} \sim n_1 N_{\text{dis}}(\tau) \sim N$. This yields finally

$$N^3 \ln(1/N) \approx \frac{F}{D}, \quad (21)$$

which coincides with the scaling law (12) for $i^* = 1$ only up to a logarithmic correction; the leading behavior of (21) for $D/F \gg 1$ is

$$N \sim (F/D)^{1/3} [\log(D/F)]^{-1/3}. \quad (22)$$

In a power law fit of N versus F/D this will tend to produce scaling exponents which are smaller than $1/3$.

The logarithmic factor can be reproduced within rate equation theory by using the expression

$$\sigma_1 \approx \frac{4\pi}{\ln[(D/F)n_1]} \sim -\frac{1}{\ln(N)} \quad (23)$$

for the capture number of adatoms [30]. Reduced rate equations of the form (6,9) which incorporate the logarithmic correction are able to quantitatively reproduce the results of kinetic Monte Carlo simulations [35].

The random walk picture has also been helpful in clarifying the case of one-dimensional diffusion. In one dimension the distance between islands is N^{-1} , and correspondingly the adatom lifetime in the steady state regime is of the order of $\tau \sim 1/(N^2D)$ and the adatom density is $n_1 \sim F/(N^2D)$. The number of distinct sites visited by a one-dimensional random walk grows as $N_{\text{dis}}(\tau) \sim \sqrt{D\tau}$. Inserting these expressions into the condition $p_{\text{nuc}} \sim N$ yields the estimate $N \sim (F/D)^{1/4}$ for $i^* = 1$ [33]. Similar considerations can be employed to derive a useful general formula for the exponent χ in the scaling law (12) [29,36]. It reads

$$\chi = \frac{di^*}{d + 2i^* + \min[di^*, 2]}. \quad (24)$$

Here $d = 1, 2$ denotes the dimensionality of diffusion. Logarithmic corrections similar to (21) arise whenever $di^* = 2$, because di^* is the effective dimensionality of the random walk in configuration space which describes the nucleation process, and two-dimensional random walks are well known to be marginally space filling [34].

3 Wedding cakes

It was first predicted by Villain [37] that the existence of step edge barriers – the fact that $D' < D$ – implies a growth instability, in which a mound morphology develops on a flat crystal surface. This phenomenon, which was subsequently observed on a variety of substrates [38–43], is the subject of the following two lectures.

3.1 Poisson growth

To appreciate the relevance of interlayer transport for multilayer growth, we first consider the case where it is completely absent, i.e. we set $D' = 0$. Then each adatom remains in the layer in which it was first deposited, and is incorporated into that layer at an ascending step edge. This implies a simple evolution of the layer coverages θ_n , $0 \leq \theta_n \leq 1$, where $n = 1, 2, 3, \dots$ counts the layers and $\theta_0 = 1$ describes the substrate. The rate at which layer n grows is proportional to the *exposed* coverage

$$\varphi_{n-1} = \theta_{n-1} - \theta_n \quad (25)$$

of the layer $n - 1$ below, and therefore the θ_n satisfy [44]

$$\frac{d\theta_n}{dt} = F(\theta_{n-1} - \theta_n) \quad (26)$$

with the initial conditions $\theta_{n \geq 1}(t = 0) = 0$. It is straightforward to check that the solution reads

$$\theta_n = 1 - e^{-\Theta} \sum_{k=0}^{n-1} \frac{\Theta^k}{k!}, \quad (27)$$

where

$$\Theta = \sum_{n=1}^{\infty} \theta_n = Ft \quad (28)$$

is the total deposited coverage. Correspondingly the exposed coverages follow a Poisson distribution with parameter Θ ,

$$\varphi_n = \frac{e^{-\Theta}\Theta^n}{n!}. \quad (29)$$

Since φ_n is the probability that an arbitrary point on the surface resides on layer n , it can also be viewed as the probability distribution of the local film height, measured in units of the layer thickness. The mean height is Θ , and the standard deviation of the φ_n defines the *surface width* W , a common measure of film roughness, through

$$W^2 = \sum_{n=0}^{\infty} (n - \Theta)^2 \varphi_n. \quad (30)$$

For the Poisson distribution (29), the variance is equal to the mean, and therefore

$$W = \sqrt{\Theta} \quad (31)$$

for growth without interlayer transport. Remarkably, the expression (31) is independent of the in-layer diffusion rate. It represents the maximum surface roughness that can be generated by the randomness in the deposition flux, and is referred to in the literature as the *statistical growth* or *random deposition* limit [12]. Interlayer transport is solely responsible for reducing the roughness below this limit.

While in-layer diffusion does not affect the *vertical* surface morphology, as encoded in the layer coverages θ_n , it is certainly reflected in the *lateral* mass distribution along the surface. This is illustrated in Figure 4 by a one-dimensional simulation. It shows the emergence of a fairly regular pattern of mound-like surface features with a characteristic pointed shape. Each mound consists of a tapering stack of islands upon islands, reminiscent of a *wedding cake*. In the following we argue that many properties of this pattern follow immediately from the expression (27) for the layer coverages [45].

Figure 4 clearly demonstrates that the lateral positions and sizes of the mounds originate in the growth of the first layer: The wedding cakes grow on the templates of the first layer islands, and their spacing is simply determined by the density N of first layer nuclei, which in one dimension is proportional to $(F/D)^{1/4}$ (see Sect.2.3). The persistence of the first layer pattern throughout the deposition of hundreds and thousands of layers requires, first, that no additional mounds nucleate during the later stages of growth, and, second, that neighboring mounds do not merge. The first requirement is met because

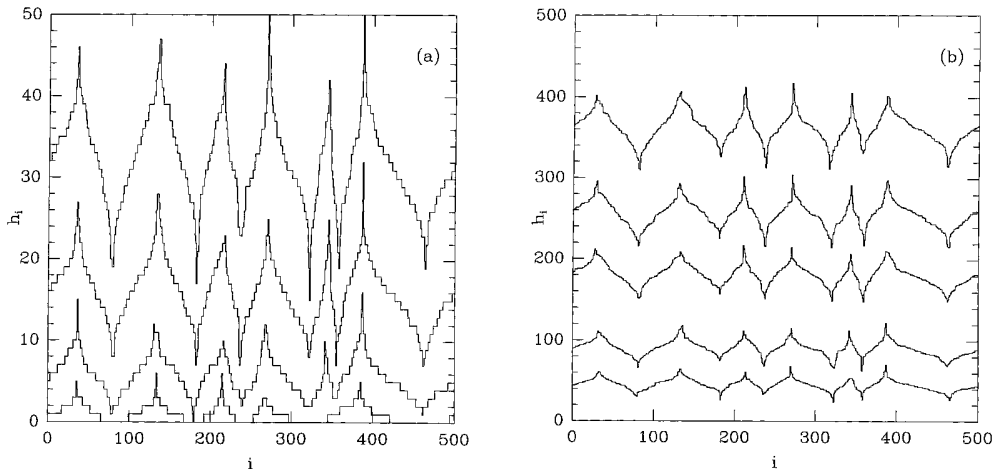


Fig. 4. Surface morphology in a one-dimensional growth model without interlayer transport. (a) Morphology after deposition of 1, 5.6, 16 and 32 monolayers. (b) Morphology after deposition of 45.25, 90.5, 181, 256 and 362 ML. The ratio of diffusion to deposition rate is $D/F = 5 \times 10^6$ [45]

the step spacing on the sides of the mounds decreases with increasing coverage (the mounds steepen), and therefore nucleation on the vicinal terraces making up the sides becomes highly unlikely. The merging of mounds is suppressed because the lateral positions of the maxima and minima of the surface profile are strongly correlated from one layer to the next. For the maxima this reflects the fact that nucleation occurs only in the top layer of each mound, while for the minima it can be attributed to the *Zeno effect*, the appearance of deep crevices between neighboring mounds [46]. Such a crevice closes very slowly, because fewer and fewer deposited atoms find their way to its bottom terrace. In particular, according to (27) the exposed fraction of the substrate $\varphi_0 = 1 - \theta_1 = e^{-\Theta}$ approaches zero only asymptotically, but does not vanish at any finite time.

The resulting picture of the pattern forming process is readily generalized to growth on real, two-dimensional substrates. The nucleation of the first layer islands partitions the substrate into capture zones. Each zone supports a single mound, which is fed by the atoms deposited into the zone. This implies that the typical shape of the mounds can be read off from the layer distribution (27): The area A_n of the n 'th layer of a mound will be equal to $\theta_n A_0$, where A_0 is the area of the corresponding capture zone. A more transparent form of (27) is obtained in the limit of thick layers, $\Theta \gg 1$, when the Poisson distribution (29) can be replaced by a Gaussian of width $\sqrt{\Theta}$. The layer distribution then follows by integration,

$$\theta_n = \Phi((n - \Theta)/\sqrt{\Theta}) \quad (32)$$

where

$$\Phi(s) = 1 - \frac{1}{\sqrt{2\pi}} \int_{-\infty}^s dy e^{-y^2/2} = \frac{1}{2}[1 - \text{erf}(s/\sqrt{2})] \quad (33)$$

and $\text{erf}(s)$ denotes the error function. Equation (32) shows that the mounds attain a time-independent limiting shape when rescaled vertically by $W = \sqrt{\Theta}$.

3.2 An improved model

The main features of the Poisson growth model agree well with deposition experiments on Pt(111) carried out for film thicknesses ranging from 0.3 to 300 ML [5] (Figure 2). The mound shape at 130 ML, obtained by averaging the layer coverages over several mounds, matches the predicted shape function (33) both in the valleys and on the slopes of the mounds, but differs significantly near the tops: Instead of the pointed peaks seen in Figure 4, the real mounds terminate in flat terraces of a characteristic lateral size (Figure 5). This discrepancy should be no surprise, since the model assumption of zero interlayer transport becomes extremely unrealistic for an adatom that has been deposited onto the freshly nucleated, small top island of a mound. In the absence of ascending step edges, such an atom has no choice but to interrogate the island edge many times and eventually cross it, even if the crossing probability in each attempt is very small. As the island grows, the residence time of the adatom increases, until the probability for two atoms to be present simultaneously on the island becomes appreciable, and a new nucleus is formed on top of the island.

We now describe a simple modification of the Poisson model which takes into account the delayed nucleation of the top layer [47]. A mound is approximated as a stack of concentric, circular islands. The base is an island of radius R_0 which does not grow, and the radius of the n 'th island is $R_n = R_0\sqrt{\theta_n}$. Since there are no sinks for atoms on the top layer, all atoms deposited there have to attach to the descending step. The top terrace therefore absorbs all atoms landing on layers n_{top} and $n_{\text{top}} - 1$, and grows according to

$$\frac{d\theta_{n_{\text{top}}}}{dt} = F\theta_{n_{\text{top}}-1}, \quad (34)$$

while (26) still applies for $n < n_{\text{top}}$. Equations (26,34) have to be supplemented by a rule for the nucleation of a new top terrace. A simple choice would be to posit that nucleation occurs whenever the current top layer reaches

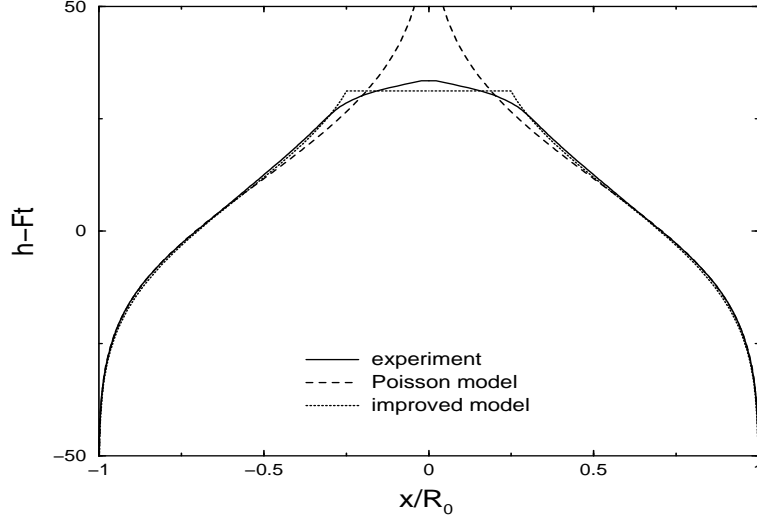


Fig. 5. Experimentally determined mean mound shape (full line) compared to the predictions of the Poisson growth model (dashed line), and a fit to the shape function in the improved model which includes nucleation on the top terrace (dotted line). The figure shows a mound composed of circular islands seen from the side. The experimental data are taken from [5], and are courtesy of T. Michely. The experimental conditions correspond to those of Figure 2 after deposition of 130 monolayers.

some critical coverage. More realistically, nucleation should be treated as a stochastic process governed by the nucleation rate ω computed in Section 2.2. A deterministic rule which is close in spirit to stochastic nucleation can be obtained as follows. Suppose the current top terrace has nucleated at time $t = 0$, and denote its radius by $R_{\text{top}}(t)$. Then the probability that no nucleation has occurred on the top terrace up to time t is given by [27]

$$P_0(t) = \exp\left(-\int_0^t dt' \omega(R_{\text{top}}(t'))\right), \quad (35)$$

and the probability density of the time t of the next nucleation event is $-dP_0/dt$. It follows that the mean value of P_0 at the time of nucleation satisfies

$$\bar{P}_0 = \int_0^\infty dt P_0(t) \left(-\frac{dP_0}{dt}\right) = 1 - \bar{P}_0 \quad (36)$$

and thus $\bar{P}_0 = 1/2$. In the numerical implementation, we therefore monitor the increase of P_0 during the growth of the top terrace and create a new top terrace when $P_0 = 1/2$. For the nucleation rate ω the expression (16) will be used.

A full analytic solution of the model is difficult because the nucleation proba-

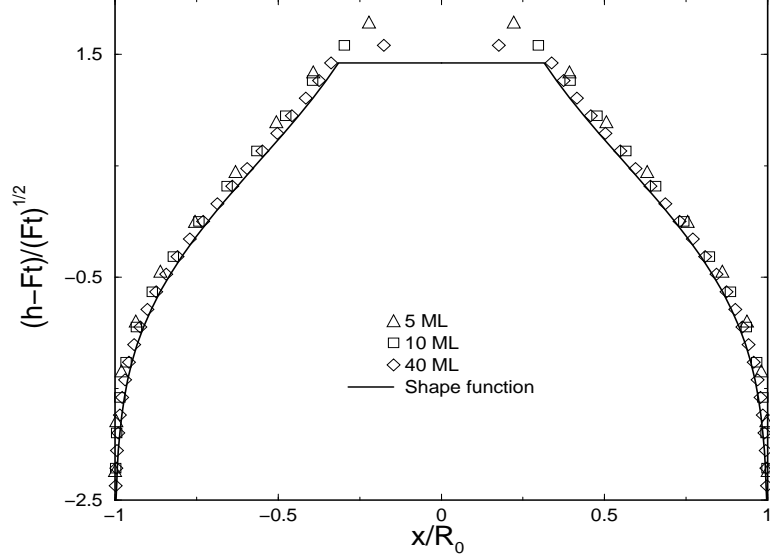


Fig. 6. Convergence of numerically generated wedding cakes to the asymptotic shape.

bility (35) depends on the size of the top terrace, which is determined by the entire history of the wedding cake through the coupled equations (26). The numerical solution of the model equations shows that, like in the case of Poisson growth, the height profile of the mound converges to a time-independent asymptotic shape, when viewed relative to the mean film height Ft and rescaled horizontally by \sqrt{Ft} (Figure 6). For large coverages this implies a separation of time scales between the mound sides, which evolve slowly at typical step velocities of order $1/\sqrt{Ft}$, and the top terrace, which reaches a coverage of order unity during the growth of one layer. It is therefore reasonable, as a first approximation, to assume that the former top terrace ceases entirely to grow once a new island has nucleated on top of it. This should produce a lower bound on the island radii reached at a given time.

Denote by R_{n-1}^{top} the radius of island $n-1$ at nucleation of island n , and by t_n the time of this nucleation event. Then during its tenure as the top terrace, the radius of island n grows, according to (34), as

$$R_n(t) = \sqrt{F(t - t_n)} R_{n-1}^{\text{top}}. \quad (37)$$

The time t_{n+1} of the next nucleation event is determined by evaluating (35) using (16) and (37), and setting the result equal to $1/2$,

$$P_0(t_{n+1}) = \exp \left(-\frac{\pi^2 F^2 (R_{n-1}^{\text{top}})^5}{2D'} \int_{t_n}^{t_{n+1}} dt [F(t - t_n)]^{5/2} \right) = 1/2. \quad (38)$$

This implies a recursion relation

$$R_n^{\text{top}} = R_c^{5/7} (R_{n-1}^{\text{top}})^{2/7} \quad (39)$$

for the size of the top terrace at nucleation of the next layer, where we have introduced the characteristic radius

$$R_c = \left(\frac{7 \ln 2}{\pi^2} \right)^{1/5} \left(\frac{D'}{F} \right)^{1/5} \approx 0.868 \cdot \left(\frac{D'}{F} \right)^{1/5}. \quad (40)$$

The time interval $\tau_n = t_{n+1} - t_n$ during which $n_{\text{top}} = n$ is related to R_n^{top} through (37), and correspondingly satisfies

$$\tau_{n+1} = F^{-1} (F \tau_n)^{4/7}. \quad (41)$$

It is easy to check that the recursion relations (39) and (41) approach fixed point values

$$R_n^{\text{top}} \rightarrow R_c, \quad F \tau_n \rightarrow 1 \quad (42)$$

exponentially fast in n . Thus asymptotically there is one nucleation event during the growth of one monolayer, and nucleation occurs when the radius of the top terrace has reached the value R_c . The numerical solution shows that these statements remain valid for the full dynamics, although the approach of R_n^{top} and τ_n to their asymptotic values is slower than exponential due to the coupling to the lower layers (the deviations decay as $1/\sqrt{Ft}$).

To derive the asymptotic mound shape analytically, we insert the ansatz (32) into (26) and expand for large Θ . We find that the shape function $\Phi(s)$ has to satisfy the differential equation

$$\Phi''(s) = -s\Phi'(s). \quad (43)$$

This shows that the inflection point of the profile, where $\Phi'' = 0$, is always located at $s = 0$, i.e. at $n = Ft$. The solution of (43) which satisfies the boundary condition $\lim_{s \rightarrow -\infty} \Phi(s) = 1$ reads

$$\Phi(s) = 1 - C[1 + \text{erf}(s/\sqrt{2})], \quad (44)$$

where C is a constant of integration. The profile is cut off at the rescaled height s_{max} of the top terrace, where the coverage takes the value $\theta_c = (R_c/R_0)^2$,

$$\Phi(s_{\text{max}}) = \theta_c. \quad (45)$$

Accordingly, the height of the top terrace above the mean film thickness Ft is $s_{\max}\sqrt{Ft}$. The Poisson shape (33) is recovered in the limit $\theta_c \rightarrow 0$, $s_{\max} \rightarrow \infty$, $C \rightarrow 1/2$.

The two parameters C and s_{\max} of the shape function are related by (45), but to fix both of them, a further relation is required. This is provided by the normalization condition (28) which, using (32), translates into

$$\int_0^{s_{\max}} ds \Phi(s) = \int_{-\infty}^0 ds (1 - \Phi(s)). \quad (46)$$

Together equations (44,45,46) define a family of shape functions parametrized by θ_c . Other features of the mound shape can be easily extracted. For example, the surface width (30) turns out to be given by

$$W^2 \approx (1 - \theta_c)Ft \quad (47)$$

asymptotically. By fitting the experimental mound shapes to the predicted shape function, the top terrace size R_c and hence, through (40), the interlayer diffusion rate D' can be determined [27]. Assuming equal preexponential factors for in-layer and interlayer diffusion, the fit shown in Figure 5 yields an additional step edge barrier of $\Delta E_S \approx 0.21$ eV.

3.3 The growth-induced current

The approach of the preceding subsections has provided us with a fairly accurate description of the shape of individual mounds. However, it does not capture global features of the morphology, such as the spatial organization of the mounds and their size distribution. Most importantly, in many (though not all [5]) experiments the mounds are observed to *coarsen*, i.e. their typical lateral extent increases with film thickness [40–43]. This requires mass transport between mounds, and hence the basic assumption of the wedding cake model – that the entire mass deposited within the capture zone of a mound contributes to its growth – cannot be upheld³. So far the only theoretical approach for treating coarsening is based on phenomenological continuum equations, which will be discussed in detail in the next section. Here our purpose is to lend some credibility to this approach by showing how the asymptotic shape of the wedding cakes can be derived within the phenomenological framework.

³ See however Sect.4.6 for a mechanism of mound coarsening without lateral mass transport.

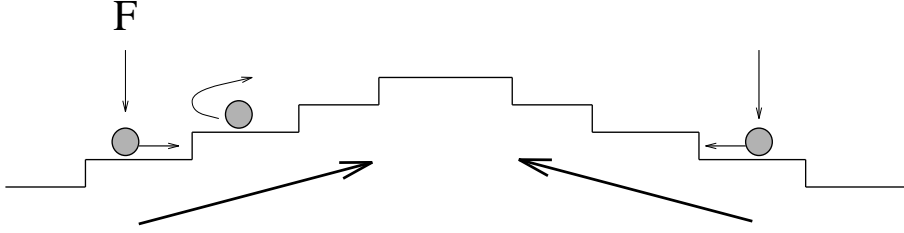


Fig. 7. Illustration of the uphill surface current generated by step edge barriers.

The continuum theory of mound formation is based on the notion of a growth-induced, uphill surface current [6,11,37,48]. Figure 7 illustrates the basic idea: Because atoms deposited onto a vicinal terrace⁴ on the side of a mound attach preferentially to the ascending step, they travel on average in the direction of the uphill slope between the point of deposition and the point of incorporation. It is important to realize that this does *not* require atoms to actually climb uphill across steps [11,48].

The evaluation of the current is particularly simple when interlayer transport is completely suppressed, and nucleation on the vicinal terrace can be neglected. An atom deposited onto a vicinal terrace of width l then travels an average distance $l/2$ to the ascending step, and hence the current is $F l/2$. Describing the surface profile by a continuous height function $h(\vec{r}, t)$ which measures the film thickness (in units of the monolayer thickness) above a substrate point \vec{r} , the local terrace width is $l = |\nabla h|^{-1}$, and hence the current is given by the expression

$$\vec{J} = \frac{F}{2|\nabla h|^2} \nabla h. \quad (48)$$

The surface profile evolves according to the continuity equation

$$\frac{\partial h}{\partial t} + \nabla \cdot \vec{J} = F. \quad (49)$$

Here we are specifically interested in radially symmetric mounds. Rewriting (49) in polar coordinates and using (48) yields the following evolution equation for the mound profile $h(r, t)$:

$$\frac{\partial h}{\partial t} = -\frac{F}{2r} \frac{\partial}{\partial r} r \left(\frac{\partial h}{\partial r} \right)^{-1} + F. \quad (50)$$

⁴ A vicinal terrace is a terrace which is bounded by an ascending step on one side and a descending step on the other. For further discussion of vicinal surfaces see Section 5.

We want to show that (50) possesses solutions corresponding to the asymptotic mound shape derived in Section 3.2. To this end we make the ansatz

$$h(r, t) = \sqrt{Ft} \psi(r) + Ft. \quad (51)$$

Inserting this into (50) yields the differential equation

$$\frac{d}{dr} \left(\frac{r}{\psi'(r)} \right) = r\psi(r). \quad (52)$$

In order to establish the equivalence between the shapes described by $\psi(r)$ and the scaled coverage distribution $\Phi(s)$ of Section 3.2, we need to verify that the function $\psi(r)$ defined implicitly by

$$\left(\frac{r}{R_0} \right)^2 = \Phi(\psi(r)) \quad (53)$$

solves (52). Indeed, taking the derivative with respect to ψ on both sides yields

$$r \left(\frac{d\psi}{dr} \right)^{-1} = -\frac{CR_0^2}{2} e^{-\psi^2/2} \quad (54)$$

which reduces to (52) upon taking another derivative with respect to r .

This calculation shows explicitly that the sides of the mounds evolve according to the continuum equation (49); in [45] the same result was obtained for a one-dimensional geometry. The continuum description does however not include the nucleation on the top terraces, which has to be added to the profile determined by (52) as a boundary condition. The development of a continuum theory of epitaxial growth which explicitly incorporates nucleation remains a challenge for the future.

4 Phenomenological continuum theory of mound formation

4.1 Motivation of the evolution equation

As it stands, the continuum equation (49) cannot be used globally, because the surface current (48) diverges for $|\nabla h| \rightarrow 0$. For small slopes the nucleation of islands on the vicinal terraces can no longer be neglected. In quantitative terms, island nucleation sets in when the width l of the vicinal terrace becomes

comparable to the distance l_D between islands nucleated on a flat surface. Using (12), the island distance is estimated as

$$l_D \approx N^{-1/2} \sim (D/F)^{\chi/2}, \quad (55)$$

with $\chi = 1/3$ for $i^* = 1$. The nucleated islands capture part of the deposited atoms, thus reducing the flux to the ascending step, and hence the uphill current. It is easy to show that the resulting net current vanishes linearly for $|\nabla h| \rightarrow 0$ [6,11]. Ignoring effects of crystal anisotropy (see Section 4.4), the current always points in the direction of ∇h . It is then generally of the form

$$\vec{J}(\nabla h) = f(|\nabla h|^2)\nabla h, \quad (56)$$

where the function $f(u)$ approaches a constant for $u \rightarrow 0$. To match the form (48) for large slope, we further require that $f \sim u^{-1}$ for $u \rightarrow \infty$. The transition between the two regimes should occur at a slope of the order of $1/l_D$. Under suitable rescaling [49] this slope, as well as all other dimensionful parameters can be set to unity, and the overall behavior of the current can be represented by the interpolation formula [39]

$$f_{\text{I}}(u) = \frac{1}{1+u} \quad (\text{model I}). \quad (57)$$

For large slopes the current functions (48) and (57) decrease indefinitely, but the uphill current remains nonzero for all slopes. This implies that mass is continuously transported uphill, leading to unbounded steepening of the morphology. Experimentally, it is often observed that the mound slopes approach a constant, “magic” value after a transient phase of steepening, a phenomenon known as *slope selection*. This can be incorporated into the continuum description by letting the current function vanish at some nonzero slope [50]. Scaling the selected slope to unity, a simple choice of the function f in (56) that incorporates slope selection is

$$f_{\text{II}}(u) = 1 - u \quad (\text{model II}). \quad (58)$$

The growth equations with current functions (57) and (58) will be referred to as model I and model II in the following.

The model defined by Eqs.(49,56) still does not constitute a useful description of the growing surface. To understand what difficulty remains, let us linearize (49) around the flat solution, writing

$$h(\vec{r}, t) = Ft + \epsilon(\vec{r}, t). \quad (59)$$

We find a diffusion equation for ϵ , but with a *negative* diffusion coefficient $-f(0)$ [37]. This confirms that the flat surface is unstable, but the instability becomes arbitrarily violent on arbitrarily short length scales. To cure this unphysical feature, we have to introduce a smoothening term which counteracts the uphill current on short length scales. Near thermal equilibrium, such smoothening is provided by the well known Gibbs-Thomson effect, which induces mass transport from positively curved regions of the surface (hilltops) to negatively curved regions (valleys). To leading order in a gradient expansion, this implies a mass current

$$\vec{J}_{\text{smooth}} = K\nabla(\nabla^2 h), \quad (60)$$

where K is proportional to the product of the surface free energy and the adatom mobility [51,52]. The Gibbs-Thomson effect may not be directly relevant under the far-from-equilibrium conditions of MBE, but other mechanisms have been suggested that give rise to a smoothening current of the same general form [6,53,54].

We follow the common practice and add the divergence of Eq.(60) to the right hand side of (49). Repeating the linear stability analysis, we find exponentially growing or decaying perturbations $\epsilon(\vec{r}, t) \sim \exp[i(\vec{q} \cdot \vec{r}) + \sigma(\vec{q})t]$, where the growth rate σ of a perturbation of wavevector \vec{q} is given by

$$\sigma(\vec{q}) = f(0)|\vec{q}|^2 - K|\vec{q}|^4. \quad (61)$$

The instability is now limited to an *unstable band* $0 < |\vec{q}| < q_c \equiv \sqrt{f(0)/K}$. Wavelengths below $2\pi/q_c$ are stabilized by the smoothening current (60). The most rapidly growing mode, which dominates the initial pattern that emerges from a generic random perturbation, has wavelength⁵ $2\pi\sqrt{2}/q_c$ and a finite growth rate $\sigma(q_c/\sqrt{2})$. The unphysical features of the instability have thus been successfully removed.

As before, the coefficient K in (60) can be set to unity by suitable rescaling. In addition, the constant deposition rate F on the right hand side of (49) can be removed by letting $h \rightarrow h - Ft$. The final outcome of these considerations is the evolution equation

$$\frac{\partial h}{\partial t} = -\nabla \cdot [f(|\nabla h|^2)\nabla h] - (\nabla^2)^2 h \quad (62)$$

which will be analyzed in the remainder of this section.

⁵ If one demands that the initial wavelength should equal the island spacing l_D , it can be shown that $K \approx Fl_D^4$ [55].

4.2 Driving force of coarsening

To gain some insight into the origin of mound coarsening, we consider the evolution of the local surface slope $\vec{m} = \nabla h$. The current (56) can be written as the negative gradient (with respect to \vec{m}) of a *slope potential* defined by

$$V(\vec{m}) = -\frac{1}{2} \int_0^{|\vec{m}|^2} du f(u). \quad (63)$$

The slope potential allows one to introduce a *Lyapunov functional* [56] for the evolution equation (62), that is, a functional of the surface morphology which is a strictly decreasing function of time. Defining

$$\Psi[h(\vec{r}, t)] = \int d^2\vec{r} \left(\frac{1}{2} (\nabla^2 h)^2 + V(\nabla h) \right), \quad (64)$$

it is a simple matter to verify that [57,58]

$$\frac{d\Psi}{dt} = - \int d^2\vec{r} \left(\frac{\partial h}{\partial t} \right)^2 < 0. \quad (65)$$

This is an extremely useful relation, because it suggests that the far-from-equilibrium growth process can be viewed in analogy to a process of relaxation to equilibrium, in which a quantity akin to a free energy is minimized.

The two terms in the integrand of (64) describe different aspects of this minimization: On the one hand, the value of the slope potential V should be minimized locally; on the other hand, the square of the surface curvature $\nabla^2 h$ should become small. The minimization of the slope potential drives the process of slope selection. It is evident from (63) that the potential has a minimum only if the function f goes through zero at some nonzero slope; otherwise, V decreases indefinitely with increasing $|\vec{m}|$, and the attempt to minimize it leads to unbounded steepening of the morphology. The minimization of the surface curvature term in (64) provides, within the continuum equation (62), the driving force for coarsening. As will be shown in the next section, this implies that the coarsening behavior depends on the spatial distribution of the curvature on the surface.

The analogy of the functional (64) to a thermodynamic free energy becomes more pronounced by writing the evolution equation for \vec{m} in the form

$$\frac{\partial \vec{m}}{\partial t} = \nabla \nabla \cdot \left(\frac{\delta \Psi}{\delta \vec{m}} \right). \quad (66)$$

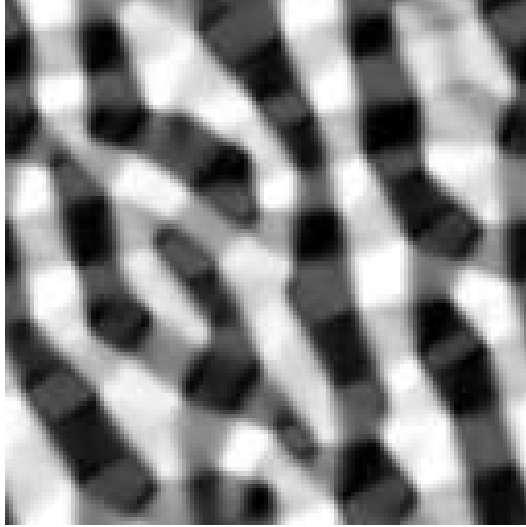


Fig. 8. Surface morphology generated by numerical solution of the growth equation (62) with slope selection (model II). Within the domains the absolute value of the slope is $|\nabla h| = 1$, and the greyscale encodes the in-plane direction of the height gradient. Maxima and minima cannot be told apart, i.e. the morphology is up-down symmetric. Courtesy of Martin Rost.

This is highly reminiscent of the Cahn-Hilliard equation, also known as model B, describing the phase ordering of a system with a two-component order parameter \vec{m} [59]. In the case of model II, the order parameter is subject to the familiar “Mexican hat” potential which favors $|\vec{m}| = 1$. Mathematically, (66) differs from model B in the ordering of the differential operators in front of the functional derivative on the right hand side, and in the fact that \vec{m} is irrotational by construction. Physically, an important difference is that the domain boundaries between regions with different orientations of the order parameter (i.e., the slope) are *straight*⁶ (Figure 8). This is in contrast to conventional phase ordering kinetics, where the domain wall curvature drives the coarsening process [57,59].

4.3 Coarsening laws

To extract the coarsening behavior from a nonlinear continuum equation such as (62), one commonly imposes a *scaling hypothesis* stating that the patterns at different times are similar, in a statistical sense, up to a rescaling by the average feature size [59]. In the present context this implies that the height-height correlation function (as well as any other statistical measure of the morphology) depends on time only through the typical lateral mound size λ

⁶ More precisely, deformations of the domain boundaries are restored on a time scale which is much shorter than the time scale for coarsening [60].

and the surface width W , and hence can be written in the form

$$\langle h(\vec{r}, t)h(0, t) \rangle = W^2(t)g(\vec{r}/\lambda(t)), \quad (67)$$

where g is a time-independent scaling function. In addition, the time dependence of λ and W is usually assumed to follow the power laws

$$\lambda(t) \sim t^n, \quad W \sim t^\beta, \quad (68)$$

which define the *coarsening exponent* n and the *roughening exponent* β . The mound slope is then of the order of $W/\lambda \sim t^{\beta-n}$. Slope selection implies $\beta = n$, while in the case of steepening $\beta > n$.

To put the scaling hypothesis to work, we consider the time evolution of the surface width. Since the mean height has already been subtracted, it is given by $W^2 = \langle h^2 \rangle$, where the angular brackets represent a spatial average. Multiplying (62) by h and integrating spatially we obtain [61]

$$\frac{1}{2} \frac{dW^2}{dt} = \langle f(|\nabla h|^2)|\nabla h|^2 \rangle - \langle (\nabla^2 h)^2 \rangle. \quad (69)$$

This clearly demonstrates how the surface is roughened (the width increased) by the uphill component of the growth-induced current, and smoothed by the curvature term in (62). Both terms on the right hand side of (69) have definite signs. Since the coarsening process can be viewed as a competition between the two terms, we expect them both, as well as their difference, to be of a similar order of magnitude⁷. This assumption is sufficient to fix the exponents n and β entering the scaling laws (68).

According to the scaling hypothesis (67), the typical curvature of the surface is of the order of W/λ^2 , and hence the right hand side of (69) can be estimated as W^2/λ^4 . This immediately leads to $n = 1/4$ independent of β . However, the estimate implicitly assumes that the curvature is *uniformly* distributed over the surface, which is true for model I (Eq.(57)) without slope selection, but not for model II (Eq.(58)). In the presence of slope selection, numerical integration of the evolution equation (62) shows that the surface breaks up into flat facets at the selected slope, $|\vec{m}| = 1$, which are separated by straight domain boundaries [58] (Figure 8). The width of these boundaries introduces

⁷ Exact calculations for one-dimensional growth equations show that this assumption may fail, because the two terms on the right hand side of (69) cancel almost completely [62,63]. The simple scaling arguments presented here then only provide upper bounds on n and β . This kind of behavior seems however to be specific to the one-dimensional geometry.

another length scale into the problem, which invalidates the naive application of the scaling hypothesis [59]. This length scale is independent of time, and coincides in order of magnitude with the initial mound size $2\pi\sqrt{2}/q_c$. The surface curvature vanishes on the facets and is concentrated in the network of domain boundaries. The correct estimate of the right hand side of (69) is therefore $\langle(\nabla^2 h)^2\rangle \sim 1/\lambda$, which yields the scaling relation $2\beta - 1 = -n$. Since slope selection also implies $\beta = n$, the result $n = 1/3$ follows for model II.

To complete the derivation for model I, we note that because of the unbounded steepening $f_I \approx |\nabla h|^{-2}$ for long times, and hence the first term on the right hand side of (69) is of order unity. Thus W^2 increases linearly in time, and $\beta = 1/2$. In summary, we have

$$n = 1/4, \beta = 1/2 \quad (\text{model I}) \quad (70)$$

$$n = \beta = 1/3 \quad (\text{model II}). \quad (71)$$

The scaling arguments for model I can be extended to equations with a smoothing term of the general form $-(-1)^k(\nabla^2)^k h$ with $k > 2$ [64]. Such terms have been proposed to model situations in which thermal detachment from steps is impossible, although no clear identification of the associated microscopic processes has been provided [41]. The second term on the right hand side of (69) then becomes $\langle(\nabla^k h)^2\rangle$, which is estimated as W^2/λ^{2k} , leading to $n = 1/2k$. The estimate of the first term remains the same as above, so that $\beta = 1/2$ independent of k .

4.4 Crystal anisotropy

Since the zeros of \vec{J} determine the stable slopes of the fully-developed mounds, the expression for the current should also incorporate the crystal symmetry of the surface [50]. To give an example, a possible choice for a surface of square symmetry reads [65]

$$\begin{aligned} J_x &= m_x(1 - m_x^2 - bm_y^2) \\ J_y &= m_y(1 - m_y^2 - bm_x^2), \end{aligned} \quad (72)$$

which generates pyramidal mounds with selected slopes

$$\vec{m}^* = \frac{(\pm 1, \pm 1)}{\sqrt{1+b}} \quad (73)$$

for $-1 < b < 1$. This reduces to the isotropic model II for $b = 1$.

The microscopic origin of the anisotropy of \vec{J} is twofold [66]. First, because of its dependence on the step structure through, for example, the density of kinks, the effective step edge barrier depends on the orientation of the step in the plane. Second, the growth-induced current contains contributions from the diffusion of atoms *along* step edges [67,68], which depend even more strongly on the step orientation. An approximate evaluation [66] of these contributions shows that it is difficult to make contact with phenomenological expressions like (72), because the microscopic analysis predicts – in contrast to (72) – that the current remains anisotropic even in the limit of small slopes, $\vec{m} \rightarrow 0$. In mathematical terms, this implies a singularity in the function $\vec{J}(\vec{m})$ at $\vec{m} = 0$, which may point to a fundamental problem of the continuum theory at small slopes.

An important consequence of crystal anisotropy is the possible breakdown of the fundamental scaling hypothesis (67) [65]. For the model (72) this occurs due to the existence of metastable checkerboard mound patterns, which coarsen only through the motion of dislocations (“roof tops”). The distance between the dislocations defines a second length scale, which is much larger than the mound size. An analysis of the dislocation dynamics suggests that $n = 1/4$, but for quite different reasons than in the case of model I. In the presence of hexagonal crystal anisotropy Eq.(71) remains valid, because the network of domain boundaries remains sufficiently disordered for the scaling arguments to apply [58].

4.5 *Up-down symmetry and desorption*

As written, Eq.(62) is symmetric under the transformation $h \rightarrow -h$, and correspondingly the morphologies it generates are up-down symmetric, that is, mounds and valleys have the same shapes. This is in strong disagreement with the mound patterns observed in experiments and Monte Carlo simulations, which display isolated mounds separated by a connected network of crevices. These morphologies can be modeled by supplementing (62) by a symmetry-breaking term [41]. In a gradient expansion, the lowest order term which accomplishes this is of the form $\nabla^2(\nabla h)^2$ [37]. For a one-dimensional evolution equation, it has been shown that such a term does not qualitatively change the coarsening behavior [62]. Since much of the analysis in this lecture relied on the introduction of the slope potential V defined in (63), which becomes impossible in the presence of a symmetry-breaking term, it is unclear if the same is true in two dimensions. In fact, it seems that the effect of the symmetry-breaking may be quite substantial: If the ridges are removed from the network of domain boundaries and only the crevices remain, it is no longer possible to localize most of the surface curvature in the domain boundaries, and the scaling arguments developed above have to be modified.

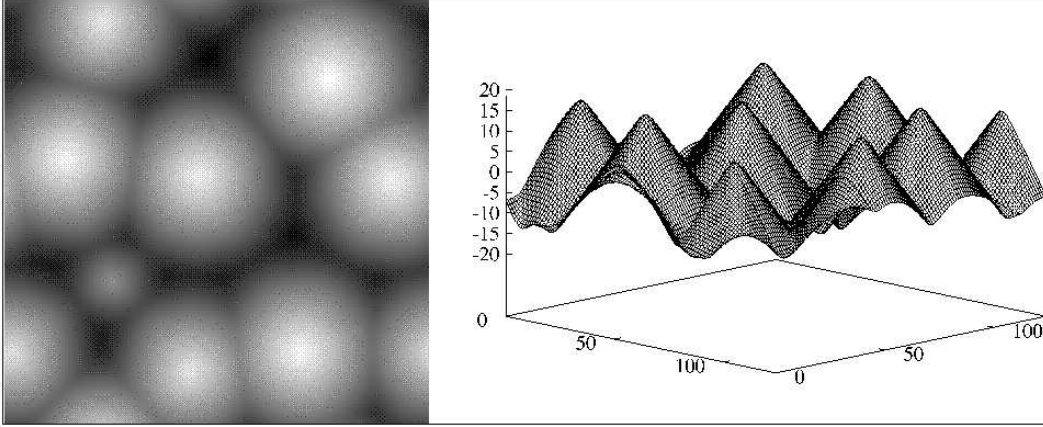


Fig. 9. Mound configurations generated by numerical solution of the evolution equation (74). Left panel shows a greyscale representation of the height. Note the distinct up-down asymmetry [69].

The up-down symmetry is also broken when desorption from the surface is allowed for. The probability for a deposited atom to redesorb from the surface before being captured at a step evidently depends on the step density, and hence on the surface slope. The desorption rate is therefore an even function of ∇h . Adding such a function to the right hand side of (62) fundamentally changes the character of the evolution equation, because the slope-dependent desorption rate cannot be written as the divergence of a current. In [69] the effect of desorption on mound coarsening was studied in the framework of the evolution equation

$$\frac{\partial h}{\partial t} = -\nabla \cdot [(1 - (\nabla h)^2)(\nabla h)] - \frac{\alpha}{1 + (\nabla h)^2} - (\nabla^2)^2 h, \quad (74)$$

where $\alpha > 0$ is a dimensionless measure of the desorption rate. The numerical integration of (74) shows the emergence of conical mounds separated by a network of crevices (Figure 9). The form of the desorption term on the right hand side of (74) implies that most desorption occurs from maxima and minima, where $\nabla h \approx 0$. Since the minima form a one-dimensional network, while the maxima (the tips of the cones) are point-like objects, the growth rate at the minima is smaller than that at the maxima by an amount of the order of $1/\lambda$, where λ is the lateral mound size. The surface width then increases according to $dW/dt \sim 1/\lambda$. Together with the slope selection property of (74) this implies $\beta = n = 1/2$. We conclude that desorption leads to a significant speedup of coarsening.

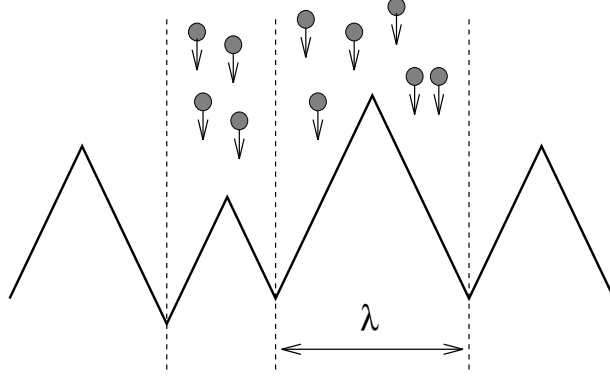


Fig. 10. Illustration of noise-induced mound coarsening.

4.6 Noise-induced mound coarsening

The theory developed so far has been entirely deterministic. Here we show that the most important source of fluctuations, the shot noise in the deposition beam, induces an alternative coarsening mechanism which generally competes with the curvature-driven coarsening described above⁸ [53,70].

The basic idea is illustrated in Figure 10. Consider an array of roughly equal sized mounds of area $A = \lambda^2$ and height $H = m\lambda/2$, where m is the mound slope. During a time t , a number FAt of atoms is deposited onto a mound, with a statistical fluctuation of $\pm\sqrt{FAt}$. If there is no mass transport between neighboring mounds, this translates into a relative height fluctuation $\delta H = \sqrt{FAt}/A$. Coarsening then occurs if, by chance, a mound overgrows a less fortunate neighbor. The condition for this to happen is that $\delta H \approx H$, which implies the coarsening law

$$\lambda \approx m^{-1/2}\Theta^{1/4}. \quad (75)$$

Under conditions of slope selection, $m = \text{const.}$, the coarsening exponent⁹ is $n = 1/4$, while in general the exponent relation

$$\beta + n = 1/2 \quad (76)$$

follows. This expresses a competition between coarsening and roughening (or steepening): The larger β , the smaller n , with the limiting case $\beta = 1/2$, $n = 0$ corresponding to the case of Poisson growth discussed in Section 3.

⁸ Quantitative analysis shows, however, that the noise-induced mechanism is negligible in most published experiments.

⁹ For a d -dimensional substrate, $n = 1/(d + 2)$.

5 Growth on stepped surfaces

The orientation of a vicinal surface is close to (in the *vicinity* of) a high symmetry direction of the crystal lattice. Such a surface therefore consists of several lattice spacings wide, high index terraces separated by steps, usually of monolayer height. During growth on a vicinal surface, the attachment of freshly deposited adatoms to the preexisting steps competes with nucleation of islands on the terraces. Nucleation is expected to be negligible if the distance l between the preexisting steps is small compared to the island spacing l_D [71] (see also Sect.4.1). The surface then maintains its vicinal shape, and growth occurs through step propagation or *step flow*. In the following the conditions for step flow will be assumed to hold¹⁰.

On a perfectly ordered vicinal surface, as it would appear in thermal equilibrium at low temperatures, the steps are straight and equally spaced. Correspondingly, the morphological instabilities of stepped surfaces are of two kinds: Either the individual steps develop a *meander*, beyond their thermal or kinetic roughness, or several steps form *step bunches*, regions of high step density separated by large terraces. The main topic of this lecture is a generic step meandering instability in homoepitaxial growth, which was first predicted theoretically by Bales and Zangwill [73]. It is caused by the asymmetry between ascending and descending steps which the step edge barrier introduces. Meandering instabilities which have been attributed to the Bales-Zangwill mechanism were identified experimentally on surfaces vicinal to Pt(111) [49] and Cu(100) [74–76]. Step bunching during homoepitaxy has been observed on several semiconductor surfaces [77,78], but a simple generic mechanism has not been suggested.

5.1 Stability of a Step Train

From a theoretical perspective, the step flow growth mode is attractive because it can be described in terms of step motion without the need to treat island nucleation. The problem simplifies further if the steps are assumed to be straight. Then the propagation speed of the j -th step in a step train can be written as the sum of the contributions f_- and f_+ from the upper and lower terraces, each of which is a function of the corresponding terrace width

¹⁰ Due to the stochastic nature of nucleation, the question about the ultimate stability of step flow is somewhat subtle [6]. For the one-dimensional Poisson growth model of Sect.3.1, it has been shown that step flow is always *metastable*, and estimates for the time scale at which it breaks down have been derived [72]. A similar breakdown has been seen in two-dimensional simulations [49], but the underlying mechanism is not clear.

(Fig.11). Denoting the position of the j -th step by x_j , the evolution equations then read

$$\frac{dx_j}{dt} = f_+(x_{j+1} - x_j) + f_-(x_j - x_{j-1}). \quad (77)$$

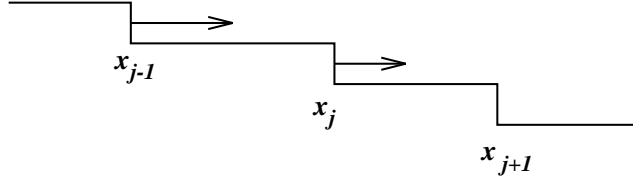


Fig. 11. Schematic of a growing step train.

A train of equally spaced steps moving at speed $v_0 = f_+(l) + f_-(l)$ evidently satisfies these equations. To probe its stability, we consider a small perturbation of the form

$$x_j(t) = jl + v_0t + \epsilon_j(t) \quad (78)$$

and linearize (77) in the ϵ_j . The solutions of the linearized equations are of the form $\epsilon_j(t) \sim \exp[i\phi j + \sigma(\phi)t]$, where the growth rate σ is given in terms of the phase shift ϕ by the expression

$$\sigma(\phi) = -(1 - \cos \phi)(f'_+(l) - f'_-(l)) + i \sin \phi (f'_+(l) + f'_-(l)). \quad (79)$$

Stability requires the real part of σ to be negative for all ϕ , which implies

$$\frac{d}{dl}(f_+(l) - f_-(l)) > 0. \quad (80)$$

Roughly speaking, (80) expresses the fact that a step train is stable if the steps are fed primarily from the lower terrace, in the sense that $f_+ > f_-$ [3]. This is easy to understand intuitively: Under this condition a step trailing a particularly wide terrace accelerates, and the uniform step spacing is restored. When (80) is violated the step train is unstable towards step bunching. The largest growth rate is then attained for $\phi = \pi$, hence step pairs form in the initial stage of the instability¹¹.

While the above analysis applies generally to growing or sublimating vicinal surfaces, we now specialize to a surface growing in the absence of evaporation. The straightforward evaluation of the functions f_{\pm} [46] then shows that a growing step train is stable whenever $D' < D$. A step bunching instability

¹¹ This need no longer be true if long ranged step-step interactions are taken into account.

during growth would require a “negative” step edge barrier, in the sense of $D' > D$. Similar arguments show that normal step edge barriers generically do cause step bunching during sublimation [3,79].

The stabilization of the equidistant step train by the step edge barrier may be interpreted in terms of an effective, growth-induced step-step repulsion. This repulsion is very efficient, in the sense that the resulting terrace width fluctuations can be far smaller than in thermal equilibrium [72,80].

5.2 The Bales-Zangwill instability

Bales and Zangwill made the remarkable observation that the very same mechanism that stabilizes a growing vicinal surface against step bunching also makes the steps susceptible to a meander instability [73]. Figure 12 illustrates the phenomenon on a qualitative level. To account for the mutual repulsion between the steps, it is assumed (and will be confirmed by the quantitative analysis) that they meander in phase. The terraces can then be subdivided into lots, as indicated by the dotted lines. Each lot receives the same number of atoms per unit time, which attach primarily to the corresponding segment of the ascending step. Because of the meander, the indented segments of the step are longer than the protruding ones. Since both capture the same flux, the protrusions propagate faster and the deformation is amplified.

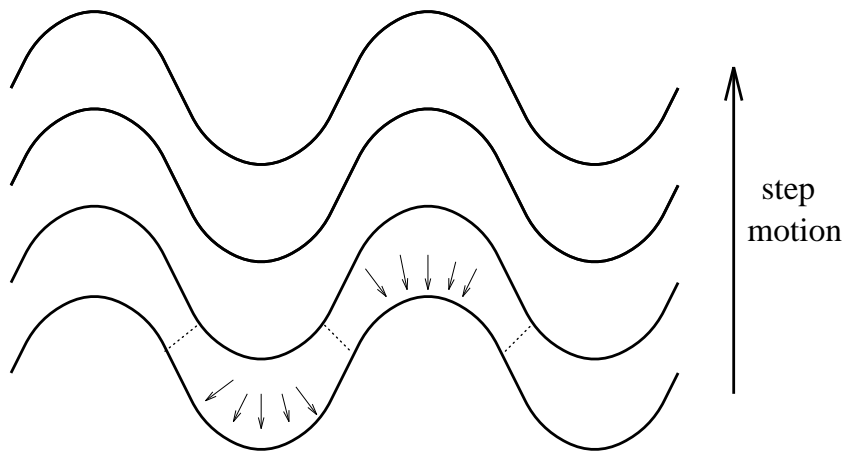


Fig. 12. Schematic of the Bales-Zangwill mechanism for step meandering

For the quantitative stability analysis, we use the coordinate system shown in Fig.13. The position of the j -th step is described by a function $\zeta_j(y, t)$. The step spacing of the unperturbed surface is l . Between the steps the adatom density $n(\vec{r}, t)$ satisfies a diffusion equation, which we employ in the stationary form

$$D\nabla^2 n + F = 0. \quad (81)$$

This is justified provided the time scale for the motion of a step across a terrace, $1/F$, is large compared to the diffusion time scale l^2/D , i.e. if the *Péclet number* [81]

$$\text{Pe} = Fl^2/D \quad (82)$$

is small compared to unity. Since the step spacing in step flow growth has to be small compared to l_D , which in turn is small compared to $(D/F)^{1/2}$ because of the relation (55), the stationarity condition is always satisfied¹².

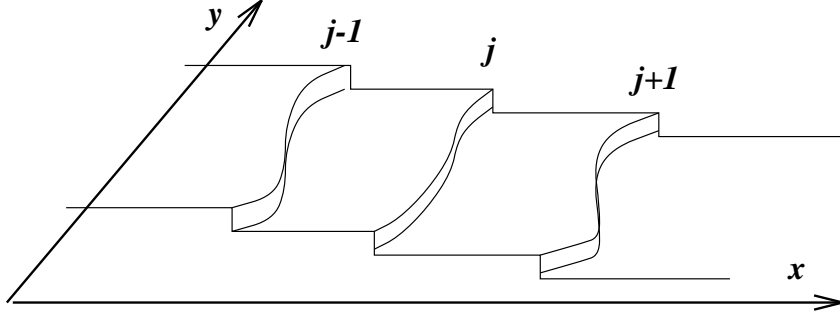


Fig. 13. Geometry of the vicinal surface used in the stability analysis.

The attachment and detachment of adatoms at the steps is described by the boundary conditions [79,81]

$$\pm D\vec{\mathbf{n}} \cdot \nabla n|_{x=\zeta_j \pm 0} = k_{\pm}(n - n_{\text{eq}}|_{x=\zeta_j \pm 0}). \quad (83)$$

Here k_+ and k_- denote the attachment rates to an ascending and a descending step, respectively, \mathbf{n} is the normal vector of the step, and \vec{n}_{eq} is the equilibrium adatom density at the step. The thermodynamic cost of step deformations enters the boundary conditions through the expression

$$n_{\text{eq}} = n_{\text{eq}}^{(0)} \left(1 + \frac{\tilde{\gamma}\kappa_{\text{st}}}{k_{\text{B}}T} \right), \quad (84)$$

where $\tilde{\gamma} = \gamma + d^2\gamma/d\vartheta^2$ is the step stiffness, related to the orientation-dependent step free energy $\gamma(\vartheta)$, $n_{\text{eq}}^{(0)}$ is the equilibrium adatom density at a straight step, and κ_{st} is the step curvature. Equation (84) is the two-dimensional analog of the Gibbs-Thomson relation mentioned in Sect.4.1.

Once the boundary value problem defined by (81,83,84) has been solved for a given configuration of steps, the local normal velocity $v_n^{(j)}$ of each step can be

¹² Step motion beyond the stationary approximation is treated in [81].

computed from the total mass flux reaching the step from the two adjoining terraces, as well as through diffusion *along* the step. This yields

$$v_n^{(j)} = D [\bar{\mathbf{n}} \cdot \nabla n|_+ - \bar{\mathbf{n}} \cdot \nabla n|_-] + \frac{\partial}{\partial s} \mu_{\text{st}} \frac{\partial}{\partial s} \tilde{\gamma} \kappa_{\text{st}}^{(j)}, \quad (85)$$

where μ_{st} is the mobility for migration along a curved (that is, atomically rough) step [52], and s denotes the arc length of the step.

The calculation now proceeds, in principle, as in Sect.5.1. The general form of the perturbed step train is

$$\zeta_j(y, t) = jl + v_0 t + \epsilon_j(y, t). \quad (86)$$

To linear order in the ϵ_j , the solution of the coupled equations can be decomposed into normal modes of the form $\epsilon_j(y, t) \sim \exp[i\phi j + i q y + \sigma(\phi, q)t]$. Here q denotes the wavenumber of the step deformation, corresponding to a meander wavelength $2\pi/q$. The real part of the growth rate $\sigma(\phi, q)$ turns out to be maximal for the in-phase mode $\phi = 0$ [82]. This is a consequence of the kinetically induced step repulsion described in Sect.5.1: The in-phase mode is a compromise which allows the deformed steps to keep the terrace width as uniform as possible.

Since the incipient morphology will be dominated by the fastest growing mode, we may assume $\phi = 0$ in the following. Moreover, for the present purposes it is sufficient to consider long wavelength deformations, with a meander wavelength large compared to the mean step spacing l . In this limit the expression for the growth rate then reads [83]

$$\sigma(0, q) = \frac{Fl^2 f_s}{2} q^2 - \left(\frac{Dn_{\text{eq}}^{(0)} l}{k_B T} + \mu_{\text{st}} \right) \tilde{\gamma} q^4. \quad (87)$$

The positive term proportional to q^2 describes the destabilization of the straight step by the attachment asymmetry. The strength of the destabilization is proportional to the flux F , and to the factor

$$f_s = \left(\frac{k_+ - k_-}{k_+ k_- \ell / D + k_- + k_+} \right) \quad (88)$$

which is a dimensionless measure of the strength of the step edge barrier. The negative term proportional to q^4 describes the thermal relaxation of the step towards the (straight) equilibrium shape. The smoothing is driven by the step stiffness $\tilde{\gamma}$, and it operates through two kinetic channels [84]: Detachment-reattachment processes over the terrace, with a rate proportional to the terrace

diffusion coefficient and the terrace width, and step edge diffusion with a rate proportional to μ_{st} .

The form of the growth rate (87) is the same that was derived in Sect.4.1 for the early stages of the mound instability (Eq.(61)), and correspondingly the physics is very similar. For sufficiently small q the quadratic term in (87) wins over the quartic term, and hence the step is subject to a long wavelength instability for arbitrarily small flux¹³. The range of unstable wavelengths is bounded below by $2\pi/q_c$, where q_c is the wavenumber at which the two terms on the right hand side of (87) balance. The dominant meander wavelength λ_{BZ} corresponds to the maximum of (87), which yields $\lambda_{\text{BZ}} = 2\pi\sqrt{2}/q_c$. Explicitly,

$$\lambda_{\text{BZ}} = 4\pi\sqrt{\frac{(Dn_{\text{eq}}^{(0)}l/k_{\text{B}}T + \mu_{\text{st}})\tilde{\gamma}}{Fl^2f_s}}. \quad (89)$$

5.3 Nonlinear step meandering

An analytic approach to the evolution of the meander instability beyond the linear regime has been developed by Misbah, Pierre-Louis and coworkers [83,85]. Since the in-phase mode is the most unstable according to linear stability analysis, the two-dimensional surface morphology can be represented by a one-dimensional function $\zeta(y, t)$ describing the displacement of the common step profile from the flat straight reference configuration $\zeta = 0$. A solvability condition arising from a multiscale expansion in $\text{Pe}^{1/2}$ then yields the evolution equation

$$\zeta_t = - \left\{ \frac{\alpha\zeta_y}{1 + \zeta_y^2} + \left(\frac{\beta}{1 + \zeta_y^2} + \frac{\beta'}{\sqrt{1 + \zeta_y^2}} \right) \left[\frac{\zeta_{yy}}{(1 + \zeta_y^2)^{3/2}} \right]_y \right\}. \quad (90)$$

Here subscripts denote derivatives, and the values of the coefficients α , β and β' can be read off by comparison with (87). The expression in square brackets is the step curvature, and the terms proportional to β and β' describe step smoothing through attachment/detachment kinetics and step edge diffusion, respectively. The form of these terms follows from simple geometric considerations [86]. The two terms differ by a factor of $\sqrt{1 + \zeta_y^2}$, because the attachment/detachment kinetics depends on the step width, while step edge diffusion does not (compare to (87)).

Two types of analytic solutions to (90) have been found [85,86]. *Stationary* solutions are obtained by setting the mass current along the step (the

¹³ In the presence of desorption, which is the case originally considered by Bales and Zangwill [73], the instability sets in only above a critical flux.

quantity inside to curly brackets on the right hand side of (90)) to zero. In terms of $m(y) = \zeta_y/\sqrt{1 + \zeta_y^2}$ the stationarity condition reduces to the oscillatory motion of a classical particle in a potential, which can be solved by quadratures. One thus obtains a one-parameter family of periodic profiles $\zeta_S(y)$ which are most conveniently parametrized by the maximum slope $S \equiv \max_y \zeta_y$. We discuss separately the special cases $\beta' = 0$ and $\beta = 0$. For $\beta' = 0$, the amplitude $A(S)$ of the profile is an increasing function of S , while the wavelength $\Lambda(S)$ decreases with increasing S , starting out at $\Lambda(0) = \lambda_c = 2\pi/q_c$. For $S \rightarrow \infty$ finite limiting values $A(\infty) = \sqrt{8\beta/\alpha}$, $\Lambda(\infty) = \sqrt{2\pi\beta/\alpha} \Gamma(3/4)/\Gamma(5/4) \approx 0.5393527.. \lambda_c$ are approached. In contrast, for $\beta = 0$ the potential is harmonic, hence the wavelength of the stationary profile is λ_c independent of its amplitude.

The *separable* solutions of interest read [45,85]

$$\zeta(y, t) = 2\sqrt{\alpha t} \operatorname{erf}^{-1}(1 - 4|y|/\lambda), \quad -\lambda/2 < y < \lambda/2, \quad (91)$$

where the wavelength λ is arbitrary. Equation (91) solves (90) exactly in the limit $t \rightarrow \infty$, when the smoothening terms on the right hand side becomes negligible compared to the first term, and the evolution equation reduces to $\zeta_t = -(\alpha/\zeta_y)_y$, the one-dimensional version of the wedding cake equation discussed in Sect.3.3. The solution (91) is highly singular near the maxima and minima, where it diverges as $\zeta \sim \pm\sqrt{\ln(1/|y - y_0|)}$, $y_0 = 0, \pm\lambda/2$.

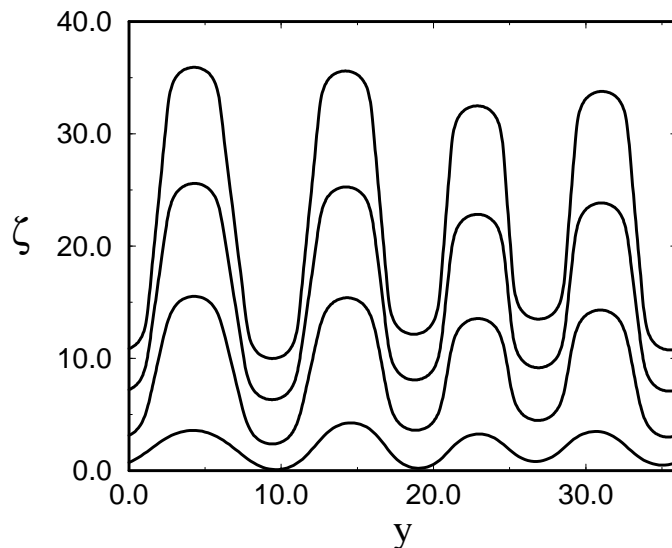


Fig. 14. Evolution of the step profile starting from a flat initial condition with small random fluctuations, for the case of pure step edge diffusion ($\beta = 0$). Subsequent profiles have been shifted in the ζ -direction. The y -axis has been scaled by λ_c .

In Figure 14 we show results of a numerical integration of (90), starting from a small amplitude random initial condition. A regular meander pattern of wavelength λ_{BZ} develops, with an amplitude growing indefinitely as \sqrt{t} . Closer inspection reveals that the sides of the profile follow the separable solution; however, the singular spikes at the maxima and minima of (91) are replaced by smooth *caps* which consist of pieces of the stationary solutions. Since the slope of (91) increases monotonically upon approaching an extremum while it decreases for the stationary profiles, the matching of the two solutions occurs near the point of maximum slope. For $t \rightarrow \infty$ the slope of the separable solution diverges, and therefore the cap profile approaches the limiting stationary solution $\zeta_{\infty}(y)$, and the length of the cap becomes $\Lambda(\infty)$. The rescaled step profile $\zeta(y, t)/\sqrt{t}$ approaches an invariant shape in which the cap appears as a flat facet.

5.4 Competing instability mechanisms

The first quantitative experimental test of the predictions of Bales and Zangwill was carried out by Ernst and collaborators for surfaces vicinal to Cu(100) [75,76]. Based on the experimentally determined dependence of the meander wavelength on temperature and flux, they concluded that their results were *not* consistent with the prediction (89). In particular, the observed flux dependence $\lambda_{\text{meander}} \sim F^{-0.2}$ differs considerably from the predicted $\lambda_{\text{BZ}} \sim F^{-1/2}$ [76].

This finding suggests that a mechanism different from the one described by Bales and Zangwill may be responsible for the step meandering on Cu(100). A plausible alternative was proposed in [67], where it was pointed out that a one-dimensional analog of the mounding instability discussed in Sections 3 and 4 should occur on a step, if the diffusion of step adatoms across “descending” kinks were suppressed by additional energy barriers. If such barriers are sufficiently strong, a one-dimensional wedding cake morphology should develop along the step, with a characteristic length scale given by the distance l_{1d} between the one-dimensional nuclei forming on the straight step in the initial stages of growth. This length scale can be estimated from one-dimensional nucleation theory (see Sect.2.3). In order of magnitude, $l_{1d} \sim (D_e/F_{1d})^{1/4}$, where D_e is the coefficient of one-dimensional diffusion along a *straight* (rather than kinked) step edge, and $F_{1d} = Fl$ is the effective flux impinging onto a unit length of the step edge. A more precise calculation yields [87]

$$l_{1d} \approx \left(\frac{12D_e}{Fl} \right)^{1/4}. \quad (92)$$

In contrast to (89), this expression is consistent with the experimental obser-

variations.

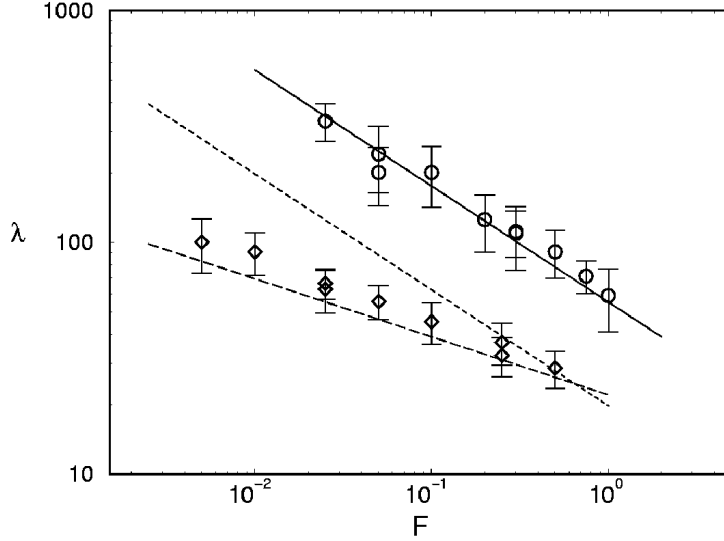


Fig. 15. Meander wavelength as a function of flux for a simple cubic solid-on-solid growth model. Diamonds and circles refer to conditions with and without facilitated edge diffusion, respectively. The full and dashed lines are the predictions of (89) and (92) for the two sets of parameters, while the dotted line shows the Bales-Zangwill prediction for the case of facilitated edge diffusion. For details on how the material parameters entering (89) and (92) are evaluated for the solid-on-solid model, see [89].

Detailed kinetic Monte Carlo simulations of stepped Cu(100) surfaces support the idea of a destabilization of the steps by kink barriers, and show wedding cake-like step profiles [88]. Simulations of a simple cubic SOS-model have moreover demonstrated that both instability mechanisms, the Bales-Zangwill scenario and the kink barrier scenario, can be observed in the same system by tuning the energy barrier for the detachment of atoms from steps [89]. When detachment is suppressed compared to edge diffusion, the kink barrier mechanism prevails, while the Bales-Zangwill instability is realized when detachment rates are comparable to edge diffusion rates. In both cases quantitative agreement with the predictions (89) and (92) can be achieved without adjustable parameters (Figure 15).

Acknowledgements

I would like to thank my collaborators Jouni Kallunki, Mirek Kotrla, Philipp Kuhn, Thomas Michely, Paolo Politi, Martin Rost and Pavel Šmilauer for fruitful and enjoyable interactions. This work has been supported by DFG within SFB 237 *Unordnung und grosse Fluktuationen*, and by Volkswagenstiftung.

References

- [1] H.Z. Cummins, in: *Fundamental Problems in Statistical Mechanics VII*, ed. by H. van Beijeren (North-Holland, 1990) p.11
- [2] G. Ehrlich, F. Hudda: *J. Chem. Phys.* **44**, 1039 (1966)
- [3] R.L. Schwoebel, E.J. Shipsey: *J. Appl. Phys.* **37**, 3682 (1966)
- [4] P. Feibelman: *Phys. Rev. Lett.* **81**, 168 (1998)
- [5] M. Kalff, P. Šmilauer, G. Comsa, T. Michely: *Surf. Sci.* **426**, L447 (1999)
- [6] P. Politi, G. Grenet, A. Marty, A. Ponchet, J. Villain: *Phys. Rep.* **324**, 271 (2000)
- [7] A. Pimpinelli, J. Villain: *Physics of Crystal Growth* (Cambridge University Press, Cambridge 1998)
- [8] I. Markov: *Crystal Growth for Beginners* (World Scientific, 1995)
- [9] Y. Saito: *Statistical Physics of Crystal Growth* (World Scientific, 1996)
- [10] J.A. Venables: *Introduction to Surface and Thin Film Processes* (Cambridge University Press, 2000)
- [11] J. Krug: *Adv. Phys.* **46**, 139 (1997)
- [12] A.-L. Barabási, H.E. Stanley: *Fractal Concepts in Surface Growth* (Cambridge University Press, 1995)
- [13] M. Kardar, G. Parisi, Y.C. Zhang: *Phys. Rev. Lett.* **56**, 889 (1986)
- [14] J. Krug, H. Spohn, in: *Solids Far From Equilibrium*, ed. by C. Godrèche (Cambridge University Press, 1991) p.479
- [15] T. Halpin-Healy and Y.C. Zhang, *Phys. Rep.* **254**, 215 (1995)
- [16] G. Palasantzas, J. Krim: *Int. J. Mod. Phys. B* **9**, 599 (1995)
- [17] H. Kallabis, L. Brendel, J. Krug, D.E. Wolf: *Int. J. Mod. Phys. B* **11**, 3621 (1997)
- [18] M. Rost, J. Krug: *J. Phys. I France* **7**, 1627 (1997)
- [19] R.S. Ross, M.F. Gyure: *Phys. Rev. B* **61**, 8602 (2000)
- [20] M. Volmer: *Kinetik der Phasenbildung* (Theodor Steinkopf, 1939)
- [21] D. Walton: *J. Chem. Phys.* **37**, 2182 (1962)
- [22] J. A. Venables: *Philos. Mag.* **27**, 697 (1973).
- [23] S. Stoyanov, D. Kashchiev, in: *Current Topics in Materials Science* ed. by E. Kaldis, Vol. 7 (North Holland, Amsterdam 1981) p.69

- [24] J. A. Venables, G. D. T. Spiller, M. Hanbücken: Rep. Prog. Phys. **47**, 399 (1984)
- [25] H. Brune: Surf. Sci. Rep. **31**, 121 (1998)
- [26] H. Brune, G. S. Bales, J. Jacobsen, C. Borragno, K. Kern: Phys. Rev. B **60**, 5991 (1999)
- [27] J. Krug, P. Politi, T. Michely: Phys. Rev. B **61**, 14037 (2000)
- [28] S. Heinrichs, J. Rottler, P. Maass: Phys. Rev. B **62**, 8338 (2000)
- [29] J. Krug: Eur. Phys. J. B **18**, 713 (2000)
- [30] G.S. Bales, D.C. Chrzan: Phys. Rev. B. **50**, 6057 (1994)
- [31] J. Tersoff, A.W. Denier van der Gon, R.M. Tromp: Phys. Rev. Lett. **72**, 266 (1994)
- [32] C. Castellano, P. Politi: Phys. Rev. Lett. **87**, 056102 (2001)
- [33] J. Villain, A. Pimpinelli, L. Tang, D. Wolf: J. Phys. I France **2**, 2107 (1992)
- [34] C. Itzykson, J.-M. Drouffe: *Statistical Field Theory*, Vol. I (Cambridge University Press, Cambridge 1989)
- [35] L.H. Tang: J. Phys. I France **3**, 935 (1993)
- [36] H. Kallabis, P.L. Krapivsky, D.E. Wolf: Eur. Phys. J. B **5**, 801 (1998)
- [37] J. Villain: J. Phys. I France **1**, 19 (1991)
- [38] H.-J. Ernst, F. Fabre, R. Folkerts, J. Lapujoulade: Phys. Rev. Lett. **72**, 112 (1994)
- [39] M.D. Johnson, C. Orme, A.W. Hunt, D. Graff, J. Sudijono, L.M. Sander, B.G. Orr: Phys. Rev. Lett. **72**, 116 (1994)
- [40] K. Thürmer, R. Koch, M. Weber, K.H. Rieder: Phys. Rev. Lett. **75**, 1767 (1995)
- [41] J. A. Stroschio, D. T. Pierce, M.D. Stiles, A. Zangwill, L.M. Sander: Phys. Rev. Lett. **75**, 4246 (1995)
- [42] F. Tsui, J. Wellman, C. Uher, R. Clarke: Phys. Rev. Lett. **76**, 3164 (1996)
- [43] J.-K. Zuo, J.F. Wendelken: Phys. Rev. Lett. **78**, 2791 (1997)
- [44] P.I. Cohen, G.S. Petrich, P.R. Pukite, G.J. Whaley, A.S. Arrott: Surf. Sci. **216**, 222 (1989)
- [45] J. Krug: J. Stat. Phys. **87**, 505 (1997)
- [46] I. Elkinani, J. Villain: J. Phys. I **4**, 949 (1994)
- [47] J. Krug, P. Kuhn, in: *Atomistic Aspects of Epitaxial Growth*, ed. by M. Kotrla, N.I. Papanicolaou, D.D. Vvedensky and L.T. Wille (Kluwer, Dordrecht 2002) cond-mat/0108262

- [48] J. Krug, M. Plischke, M. Siegert: Phys. Rev. Lett. **70**, 3271 (1993)
- [49] M. Rost, P. Šmilauer, J. Krug: Surf. Sci. **369**, 393 (1996)
- [50] M. Siegert, M. Plischke: Phys. Rev. Lett. **73**, 1517 (1994)
- [51] W.W. Mullins: J. Appl. Phys. **30**, 77 (1959)
- [52] J. Krug, H.T. Dobbs and S. Majaniemi, Z. Phys. B **97**, 281 (1995).
- [53] L.-H. Tang, P. Šmilauer, D.D. Vvedensky: Eur. Phys. J. B **2**, 409 (1998)
- [54] Th. Michely, M. Kalff, G. Comsa, M. Strobel, K.-H. Heinig: Phys. Rev. Lett. **86**, 2589 (2001)
- [55] J. Krug: Physica A **263**, 170 (1999)
- [56] P. Manneville: *Dissipative Structures and Weak Turbulence* (Academic Press, San Diego 1990)
- [57] M. Siegert: Physica A **239**, 420 (1997)
- [58] D. Moldovan, L. Golubovic: Phys. Rev. E **61**, 6190 (2000)
- [59] A.J. Bray: Adv. Phys. **43**, 357 (1994)
- [60] M. Siegert, M. Plischke, R.K.P. Zia: Phys. Rev. Lett. **78**, 3705 (1997)
- [61] M. Rost, J. Krug: Phys. Rev. E **55**, 3952 (1997)
- [62] P. Politi: Phys. Rev. E **58**, 281 (1998)
- [63] P. Politi, A. Torcini: J. Phys. A **33**, L77 (2000)
- [64] L. Golubović: Phys. Rev. Lett. **78**, 90 (1997)
- [65] M. Siegert: Phys. Rev. Lett. **81**, 5481 (1998)
- [66] P. Politi, J. Krug: Surf. Sci. **446**, 89 (2000)
- [67] O. Pierre-Louis, M. R. D’Orsogna, T.L. Einstein: Phys. Rev. Lett. **82**, 3661 (1999)
- [68] M.V. Ramana Murty, B.H. Cooper: Phys. Rev. Lett. **83**, 352 (1999)
- [69] P. Šmilauer, M. Rost, J.Krug, Phys.Rev. E **59**, R6263 (1999)
- [70] J. Krug, in: *Nonequilibrium Statistical Mechanics in One Dimension*, ed. by V. Privman. (Cambridge University Press, Cambridge 1997) p.305
- [71] A. Pimpinelli, P. Peyla: Int. J. Mod. Phys. B **11**, 3647 (1997)
- [72] J. Krug, M. Schimschak: J. Phys. France I **5**, 1065 (1995)
- [73] G.S. Bales, A. Zangwill: Phys. Rev. B. **41**, 5500 (1990)
- [74] L. Schwenger, R.L. Folkerts, H.-J. Ernst: Phys. Rev. B **55**, R7406 (1997)

- [75] T. Maroutian, L. Douillard, H.-J. Ernst: Phys. Rev. Lett. **83**, 4353 (1999)
- [76] T. Maroutian, L. Douillard, H.-J. Ernst: Phys. Rev. B **64**, 165401 (2001)
- [77] C. Schelling, G. Springholz, F. Schäffler: Phys. Rev. Lett. **83**, 995 (1999)
- [78] P. Tejedor, P. Šmilauer, C. Roberts, B.A. Joyce: Phys. Rev. B **59**, 2341 (1999)
- [79] R.L. Schwoebel: J. Appl. Phys. **40**, 614 (1969)
- [80] O. Pierre-Louis, C. Misbah: Phys. Rev. B **58**, 2259 (1998)
- [81] R. Ghez, S.S. Iyer: IBM J. Res. Dev. **32**, 804 (1988)
- [82] A. Pimpinelli, I. Elkinani, A. Karma, C. Misbah, J. Villain: J. Phys. Condens. Matter **6**, 2661 (1994)
- [83] F. Gillet, O. Pierre-Louis, C. Misbah: Eur. Phys. J. B **18**, 519 (2000)
- [84] A. Pimpinelli, J. Villain, D. E. Wolf, J. J. Métois, J. C. Heyraud, I. Elkinani, G. Uimin: Surf. Sci. **295**, 143 (1993)
- [85] O. Pierre-Louis, C. Misbah, Y. Saito, J. Krug and P. Politi: Phys. Rev. Lett. **80**, 4221 (1998).
- [86] J. Kallunki and J. Krug: Phys. Rev. E **62**, 6229 (2000)
- [87] P. Politi: J. Phys. I France **7**, 797 (1997)
- [88] M. Rusanen, I. T. Koponen, J. Heinonen and T. Ala-Nissila: Phys.Rev.Lett. **86**, 5317 (2001)
- [89] J. Kallunki, J. Krug and M. Kotrla: Phys. Rev. B **65**, 205411 (2002)